Article

Not peer-reviewed version

Solid State Additive Manufacturing of Thermoset Composites

Bo Hong , Kaifeng Wang * , Yang Li , Shuhan Ren , Peihua Gu

Posted Date: 24 July 2024

doi: 10.20944/preprints202407.1924.v1

Keywords: Cold spray; Additive manufacturing; Thermosets

Article

Solid State Additive Manufacturing of Thermoset Composites

Bo Hong [1,2], Kaifeng Wang [1,3,*], Yang Li [4,*], Shuhan Ren [3] and Peihua Gu [1,3]

[1] Key Laboratory of Mechanism Theory and Equipment Design of Ministry of Education, Tianjin University, Tianjin 300354, CHN; bhong@stu.edu.cn (B.H.); peihua.gu@tju.edu.cn (P.G.)
[2] Intelligent Manufacturing Key Laboratory of Ministry of Education, Shantou University, Shantou 515063, CHN
[3] International Institute for Innovative Design and Intelligent Manufacturing of Tianjin University in Zhejiang, Shaoxing 312000, CHN; 931386673@qq.com (S.R.)
[4] School of Materials Science and Engineering, Tianjin University, Tianjin 300354, CHN
* Correspondence: wangkf@tju.edu.cn (K.W.); liyang86@tju.edu.cn (Y.L.)

Abstract: This paper proposes an innovative approach to address the challenge of softening deformation of thermal-curable thermosets during additive manufacturing. This approach involves the development of a composite powder composed of thermosetting materials with distinct curing temperatures, the utilization of Cold Spray Additive Manufacturing (CSAM) technology for 3D printing, and the application of a stepwise isothermal curing process. The corresponding effectiveness is validated by case studies. The results demonstrate that samples printed via CSAM maintain a solid state without deformation. During the post-curing process, each component of the composite material cures independently while the other components remain in a solid state, providing structural support for the whole material, thereby effectively reducing the softening deformation during the post-curing process. This approach offers a novel perspective for the additive manufacturing of thermal-curable thermosets.

Keywords: cold spray; additive manufacturing; thermosets

1. Introduction

Thermosetting materials have garnered significant attention in various industries, including aerospace, automotive, and electronics, due to their exceptional mechanical properties and chemical stability [1–3]. In recent years, there has been increasing interest in additive manufacturing of thermosetting materials, with photocurable resins at the forefront of this research trend [4,5]. However, the exploration of thermal-curable thermosets in additive manufacturing remains relatively underexplored.

One of the primary challenges in additive manufacturing of thermal-curable thermosets is their tendency to soften and deform [6]. This problem can arise both during the 3D-printing process and the subsequent heat curing stages. Some traditional additive manufacturing methods rely on the deposition of liquid materials, such as Material Jetting (MJ) [7,8], Direct Ink Writing (DIW) [9,10], and Liquid Deposition Modeling (LDM) [11]. The inherent mechanical weakness of liquid materials makes 3D-printed structures easily deform under their own weight or external forces. This problem is particularly pronounced in materials with slow curing rates, as prolonged curing time increases the likelihood of deformation.

In addition, conventional additive manufacturing techniques using solid materials, including Fused Deposition Modeling (FDM) [12,13], Selective Laser Sintering (SLS) [14,15], and Fused Granular Fabrication (FGF) [16,17], typically involve rapid melting, liquid-state deposition, and rapid solidification of materials. In cases where complete curing is not achieved during the rapid

 doi:10.20944/preprints202407.1924.v1

solidification phase, subsequent heat treatment should be performed. However, this additional heating process can lead to further melting and deformation of the printed structures.

To address these challenges, an innovative three-step approach is proposed in this paper. Firstly, a composite powder material by combining multiple thermosetting materials with distinct curing temperatures is prepared. Secondly, Cold Spray Additive Manufacturing (CSAM), a technique that utilizes high-velocity particle impact for material deposition [18,19], is adopted, which can maintain the deposited material in a solid state throughout the 3D-printing process [20,21]. Finally, a stepwise isothermal curing process is implemented, allowing the different components of the composite powder to melt and cure sequentially at different temperatures. This strategy ensures that only partial melting occurs in the overall material, thereby controlling deformation.

To validate the efficacy of this approach, a case study is conducted using two thermosetting powders, P1 and P2, and their composite powder C. Cylindrical samples are fabricated using CSAM technology and subsequently subjected to stepwise curing. The results demonstrate that the samples maintain their original shape throughout both the additive manufacturing process and the heat curing stages. Notably, the composite material C not only preserves its shape stability but also achieves complete curing in significantly less time compared to traditional low heating rate curing methods, thereby substantially enhancing production efficiency.

2. Materials and Methods

2.1. Materials

Two commercial bisphenol-A epoxy resin powders and their corresponding latent curing agents were utilized to prepare thermosetting powders in this paper. The epoxy resins were designated as E50 and E57, while the curing agents were labeled as A80 and A95. Both the epoxy resin and the curing agents exhibited average particle sizes within the range of 3~5 μm. The epoxy equivalent weight (EEW) of E50 was 0.09~0.14 mol/100g, whereas E57 had an EEW range of 0.05~0.06 mol/100g. A80 and A95 were activated after melting and undergo curing reactions with epoxy resin.

The epoxy resins and curing agents were combined to create two distinct thermosetting powders, named P1 and P2. To ensure a significant difference in melting points between P1 and P2, thermomechanical analysis (TMA) was conducted on the resin and curing agent powders, as depicted in Figure 1. It can be seen that E50 and A80 exhibit similar melting ranges, as do E57 and A95. Consequently, E50 was paired with A80 to form P1, while E57 was paired with A95 to form P2. Both A80 and A95 were latent curing agents that activated upon melting, resulting in distinct activation temperatures for P1 and P2. According to the manufacturer's technical data, the mass ratio of E50 to A80 in P1 was 4:1, and the same ratio was applied for E57 and A95 in P2.

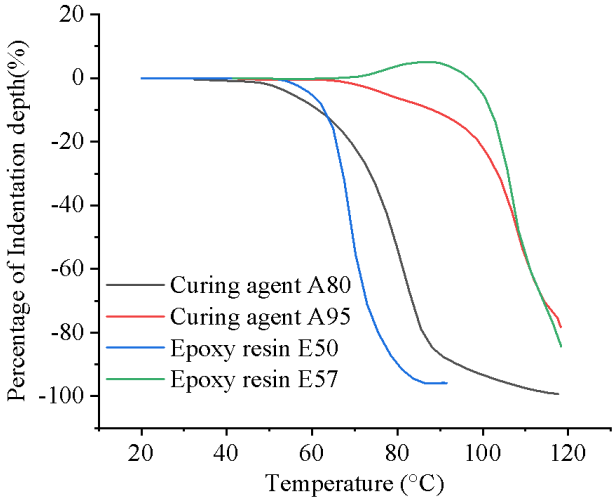

Figure 1. TMA of the as-received powder conducted at a constant heating rate of 10 °C /min.

 doi:10.20944/preprints202407.1924.v1

2.2. Powder Fabrication Process

The preparation of the powders was conducted in two distinct stages. Initially, single-component thermosetting powders P1 and P2 were fabricated using E50, E57, A80, and A95. Subsequently, composite powder C was fabricated by combining P1 and P2, as illustrated in Figure 2. The fabrication of P1 and P2 involved several steps. Firstly, the epoxy resins and curing agents were mixed and then compressed at room temperature using a hydraulic press. The compressed material was subsequently pulverized in water and subjected to a drying process. The preparation of the composite powder C followed a similar procedure. P1 and P2 powders were mixed, compressed, and then pulverized in water. Composite powder C was composed of a 1:1 volumetric ratio of P1 and P2. To prevent premature curing reactions during powder preparation, all operations were conducted at room temperature. Figure 2 depicts the irregular shapes of the resulting P1, P2, and C powder particles. The average particle diameters of P1, P2, and C were within the range of 45~50 μm.

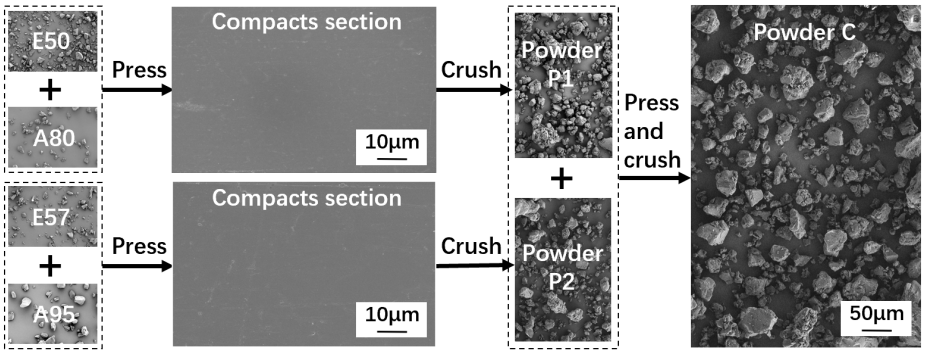

Figure 2. The powder fabrication process.

2.3. 3D Printing Procedure

CSAM was conducted using a customized low-pressure cold spray system, as illustrated in Figure 3. The powders were controlled using a vibratory feeder and introduced into the nozzle, which has an exit diameter of 5 mm. The powders were then accelerated by air pressurized to 0.8 MPa and then deposited onto a nylon-66 sheet substrate.

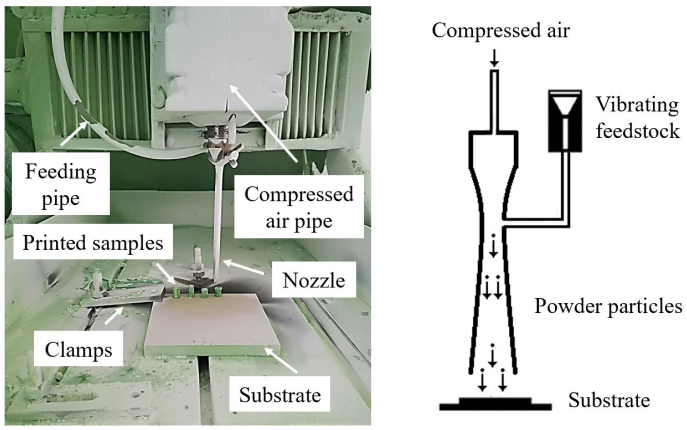

Figure 3. Cold spray system setup and schematic of CSAM process.

Cylindrical samples were fabricated with the CSAM process. The nozzle was fixed at a specific point on the substrate for cold spraying. The nozzle movement was controlled vertically, facilitating the layer-by-layer construction of the cylindrical samples. Throughout the printing process, a consistent stand-off distance of 10 mm was maintained between the nozzle exit and the top surface of the samples being deposited. The printing of cylindrical samples for P1, P2, and C was carried out at room temperature.

 doi:10.20944/preprints202407.1924.v1

2.4. Curing Process

Thermal curing was performed on the 3D printed samples, and two distinct curing methods were utilized to evaluate the impact of different curing processes on material deformation. The first method controlled the softening deformation by adjusting the heating rate. Based on the manufacturer's data, a rapid heating rate of 2 °C/min and a slow heating rate of 0.1 °C/min were selected, with the heating temperature ranging from 50~150 °C. The impact of these heating rates on material deformation was then compared. The second method utilized a stepwise isothermal curing process to control the softening deformation by sequentially curing P1 and P2. To determine the appropriate heating temperatures, TMA was performed on P1, P2, and C, as depicted in Figure 4. Significant deformation was observed for P1 and P2 at temperatures exceeding 75 °C and 90 °C, respectively, indicating the onset of melting and curing. Consequently, the first isothermal heating temperature was set at 85 °C to ensure the curing of P1 while keeping P2 in a solid state. Once P1 was fully cured, the temperature was elevated to 150 °C to facilitate the rapid curing of P2.

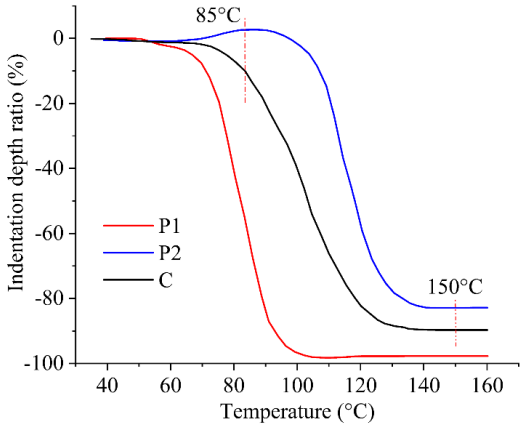

Figure 4. TMA of the prepared thermoset powder conducted at a constant heating rate of 10 °C /min.

To determine the heating duration for each stage, Vickers hardness measurements were conducted to assess the degree of curing, as shown in Figure 5. The Vickers hardness of P1 and P2 remained constant approximately after specific heating time, indicating the completion of the curing reaction. Therefore, the process for determining the stepwise isothermal curing procedure is as follows: Initially, heating was conducted at 85 °C for 1 h, followed by heating at 150 °C for 30 mins. Prior to reaching the constant heating temperature, a ramp-up rate of approximately 20.1 °C/min was employed. The detailed heating schedule is illustrated in Figure 6.

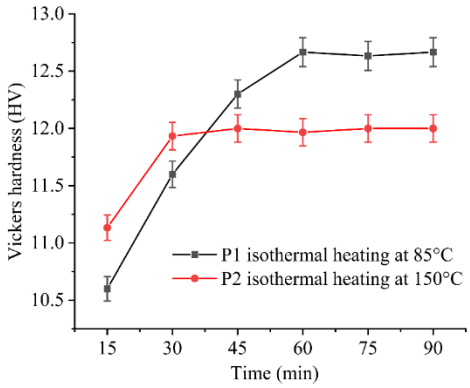

Figure 5. The evolution of Vickers hardness with heating time under isothermal heating for P1 and P2.

 doi:10.20944/preprints202407.1924.v1

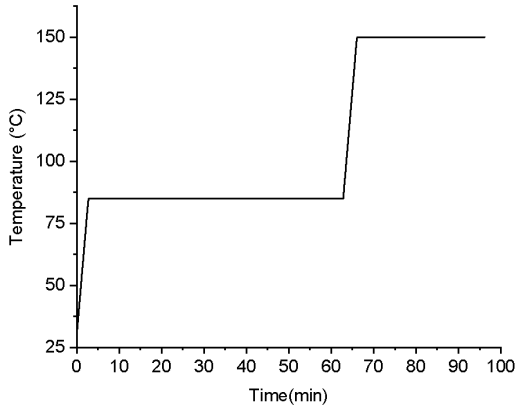

Figure 6. The stepwise isothermal heating process.

2.5. Experimental Characterization

2.5.1. Microstructural Analysis

The surface features and fracture surface morphologies of the thermosetting powders and cold-sprayed samples were characterized using a scanning electron microscopy.

2.5.2. Mechanical PROPERTY ANALYSIS

To evaluate the changes of mechanical properties, the Vickers microhardness was assessed. The tests were performed using the Model HV-1000B microhardness tester under an applied load of 10 gf for a dwell time of 15 s, in accordance with the ASTM E384-17 standard [22]. Three random regions without pores were tested for each sample to ensure accuracy and reliability of the measurements. The hardness testing of powder materials was conducted prior to the crushing stage in the powder fabrication process.

2.5.3. Thermo-Property Analysis

Differential scanning calorimetry (DSC) was employed to investigate the thermal properties and curing behavior of the printed samples, including P1, P2, and C, both before and after the stepwise heating conditions. The analysis was conducted using a Shimadzu DSC-60 instrument under nitrogen atmosphere with samples were subjected to a temperature range of 25~200 °C at a heating rate of 10 °C/min.

In addition, TMA was conducted to investigate the material deformation at varying temperatures. The test samples were circular discs with a diameter of 20 mm and a thickness of 1~2 mm, fabricated from powder material and shaped using hydraulic pressing. The samples were placed on a programmable heated plate. During the test, a constant load of 20 g was applied using a spherical indenter with a diameter of 5 mm. For the softening range assessment, a heating rate of 10 °C/min was employed. When evaluating deformation under a stepwise isothermal curing process, the heating program depicted in Figure 6 was utilized. Throughout the TMA test, the indentation depth at different temperatures was recorded. The material deformation was characterized by the ratio of the indentation depth to the sample thickness.

3. Results and Discussion

3.1. Deposited Sample Morphology Analysis

Cylindrical samples were printed using CSAM technology with powders P1, P2, and C, as depicted in Figure 7a,e,i. These samples, with heights ranging from 6 mm to 12 mm and diameters approximately 5.5 ± 0.5 mm, close to the nozzle diameter of 5 mm. The surface of the cylindrical

 doi:10.20944/preprints202407.1924.v1

samples exhibited a "wrinkled" structure, indicating instability during powder deposition and subsequently resulting in a change in deposition diameter. In addition, these parallel wrinkles suggest a consistent layer-by-layer deposition.

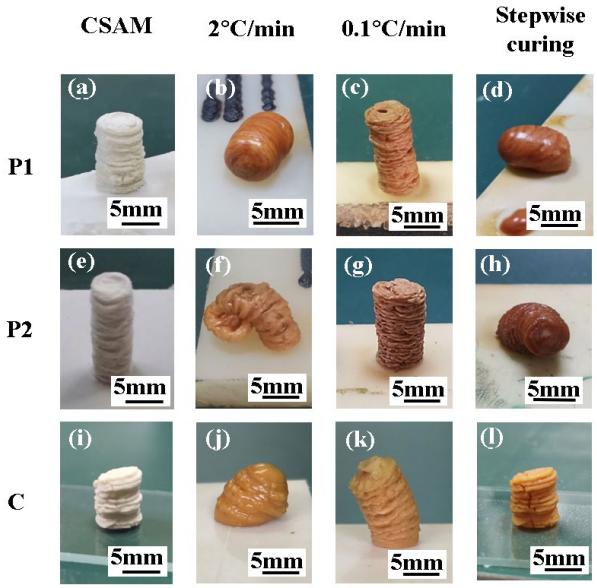

Figure 7. The morphology evolution of printed samples with different heating processes. (a)-(d) The morphology evolution of P1. (e)-(h) The morphology evolution of P2. (i)-(l) The morphology evolution of C.

It is noteworthy that the deposition rates of powders P1, P2, and C in CSAM are 5%, 2.1%, and 3.5%, respectively, where the deposition rate is defined as the ratio of the mass of the powder material deposited on the substrate to the total mass of the powder spraying during the CSAM process. Due to the varying deposition rates of P1 and P2, spraying a mixture of these powders does not produce a deposited material in P1 and P2 proportions consistent with the original powder mixture. To mitigate the effects of these differences in deposition efficiency, this study utilized a compaction method to bond P1 and P2 relatively together to produce powder C.

Subsequently, the cylindrical samples were subjected to two distinct curing processes for curing. The first method was conducted by controlling the heating rate. As illustrated in Figure 7b,f,j, the samples printed using P1, P2, and C experienced significant softening deformation at a high heating rate of 2 °C/min. Conversely, when the heating rate was reduced to 0.1 °C/min, as illustrated in Figure 7c,g,k, the samples almost retained the cylindrical shape, although the heating duration extended to 16.7 h.

The second method utilized a stepwise isothermal curing process, as depicted in Figure 6, to sequentially cure the components and manage the deformation. Figure 7d,h illustrate that samples printed using P1 and P2 softened at their respective isothermal conditions of 85 °C and 150 °C. In contrast, the sample printed using C, as shown in Figure 7l, did not display any softening deformation with the stepwise curing process. It retained the cylindrical shape and the wrinkled surface texture observed in the initial morphology depicted in Figure 7i. Moreover, it is found that the corresponding stepwise curing process required only 1.5 h, significantly less than the time required by the low heating rate method (i.e., 16.7 h).

Therefore, employing composite powder material C for CSAM printing and combining with a stepwise curing process can significantly mitigate the deformation issue both during the 3D-printing and curing stages.

3.2. Deposition and Curing Mechanism Analysis

During the CSAM process, thermosetting powders P1, P2, and C can be successfully deposited at room temperature. At this temperature, P1, P2, and C are in a glassy state, exhibiting brittle

 doi:10.20944/preprints202407.1924.v1

characteristics. Traditionally, brittle materials have significant challenges for CSAM applications, primarily due to their tendency to fracture upon impact, which normally results in thin films rather than substantial deposits [23,24]. However, the CSAM samples printed using P1, P2, and C demonstrated the ability to form cylindrical structures, indicating their potential for additive manufacturing applications. Thus, the deposition mechanism of P1, P2 and C should be significantly different from that of other brittle materials.

To investigate the corresponding deposition mechanism of thermosetting powders during the CSAM process, the particle impact velocity was estimated firstly. The average particle velocity of P1, P2, and C powders at the nozzle exit was in the range of 378~387 m/s, as predicted with the one-dimensional steady gas-dynamic model [25,26]. This high velocity provided the necessary conditions for severe plastic deformation of the particles upon impact. The surface morphologies of the samples printed using P1, P2, and C were examined, as shown in Figure 8. A number of sharp ridges and valleys were observed, indicating that the heat generated during impact was insufficient to cause complete melting of the whole particle.

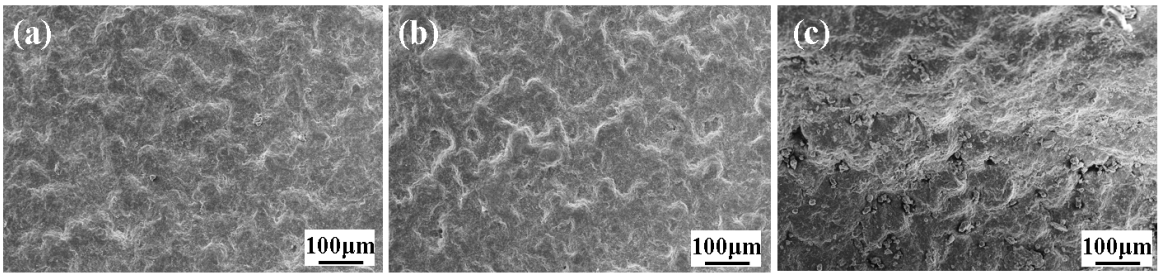

Figure 8. Surface morphologies of the samples printed using (a) P1, (b) P2, and (c) C.

Meanwhile, the fracture surface of the samples printed using P1 and P2 was observed, as shown in Figure 9a,b. It can be seen that the original form of the powder particles was no longer recognizable, and the contact interface between particles was also indistinguishable, indicating severe plastic deformation had occurred during the powder deposition. Additionally, a number of pores were found throughout the fracture surface of the samples, which could be categorized into two types based on their shapes, i.e., irregular pores with diameters close to 20 μm and small round pores with diameters of a few micrometers. Similar to the cold spraying of metal powders [27,28], air could be trapped during the powder deposition process, leading to the formation of the large irregular pores. For the dense small circular pores, they should be generated during the impact of the particles. Our prior research indicates that particles deposited onto surfaces display lower melting peaks in DSC compared to the original powder particles [29]. This observation suggests that local melting occurred during impact, activating latent curing agents and accompanying release of blocking agents, where gas was generated during the decomposition or volatilization of the blocking agent to form the small circular pores [30]. Hence, the presence of these micro-sized pores implies that particle melting occurred at the impact surface.

Based on above observations, the deposition mechanism of P1, P2 and C is due to the severe plastic deformation caused by high-speed particle impact, accompanied by significant heat generation. This thermal effect leads to local melting of the particle impact zone and transition from glassy state to viscous flow dynamic. Consequently, fusion occurs at the contact surface of the particles, promoting a strong bond, while also leading to the formation of small pores on the fracture surface.

 doi:10.20944/preprints202407.1924.v1

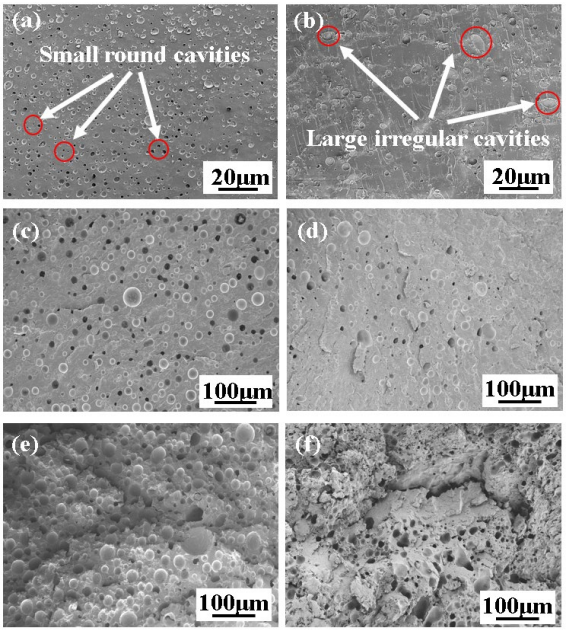

Figure 9. Fracture surface of the samples printed using P1 and P2 (a)-(b) before heating; (c)-(d) after the first heating at 85 °C for 1 h; (e)-(f) after the second heating at 150 °C for 0.5 h.

To analyze the changes of the two components P1 and P2 in composite materials C during stepwise isothermal curing, the fracture surface of the samples, printed using P1 and P2, before and after heating was observed. Figure 9c,d display the fracture morphologies of the samples after the first stage of heating. After heating at 85 °C for 1 h, in addition to small circular pores, there are also large circular pores with diameters in the range of tens of microns for the samples printed using P1. This indicates that the latent curing agent decomposed during heating, releasing a significant amount of gas, which expanded the pores as the epoxy resin melted. In contrast, the number of large pores in the samples printed using P2 was significantly less than that in the samples printed using P1, and some of the pores are irregular in shape. This may be attributed to the fact that no significant curing reaction occurs in the samples printed using P2, and most of the curing agents had not decomposed to generate gas.

Figure 9e,f show the fracture morphologies of the samples printed using P1 and P2 after the second stage of heating. The fracture surface of the samples printed using P1 displayed more large pores compared with the first stage of heating. This could be attributed to that the latent curing agent further decomposed at higher temperatures, producing more gas and forming more large pores. Similarly, the fracture surface of the samples printed using P2 also exhibited more large pores after the second stage of heating.

In addition, to investigate the effect of stepwise isothermal curing on the thermal properties, DSC tests were conducted on the samples printed using P1 and P2. As shown in Figure 10, the DSC curves of P1 and P2 before heating exhibited significant endothermic peaks at around 55 °C and 70 °C, indicating the existence of crystallization in the epoxy resin. In addition, significant exothermic peaks suggest that the samples did not complete the curing reaction during the CSAM process, indicating the need for post-heating curing treatment.

 doi:10.20944/preprints202407.1924.v1

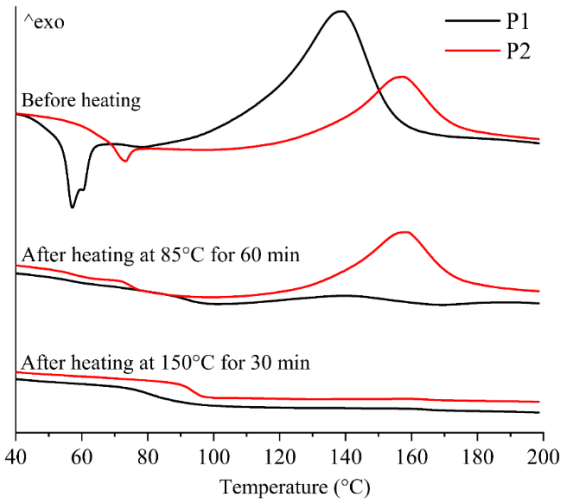

Figure 10. DSC curves of the printed samples printed using P1 and P2.

After heating at 85 °C for 1 h in the first stage, the endothermic peak of P1 disappeared, and the exothermic peak significantly decreased, indicating that the curing reaction of P1 had been essentially completed in the first heating stage. In contrast, the endothermic peak of P2 disappeared, while the exothermic peak only showed slight changes, suggesting that the curing of P2 was not significantly activated in the first stage. After heating at 150 °C for 30 mins in the second stage, the exothermic peak of P2 disappeared, indicating that the curing reaction of P2 was completed during the second stage of heating.

From above analysis, it can be confirmed that the stepwise curing process induces sequential curing reactions of P1 and P2. During these curing reactions, gas is generated, leading to the formation of a porous structure.

3.3. Mechanical Property Evaluation

To investigate the influence of stepwise isothermal heating on the mechanical properties of the printed samples, TMA was conducted by using the proposed heating program illustrated in Figure 6. Figure 11 presents the changes of the indentation depth ratio of the samples printed using P1, P2 and C during the stepwise isothermal heating process, where the indentation depth ratio is defined as the ratio of the indentation depth to the thickness of the tested sample, to evaluate the sample deformation.

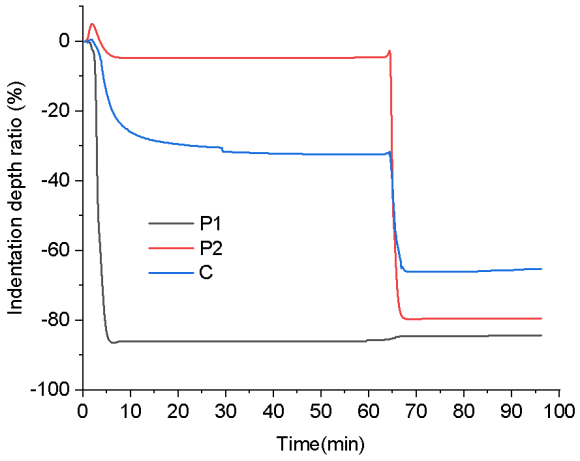

Figure 11. TMA of the printed samples with the stepwise isothermal heating process.

From Figure 11, it can be seen that the sample printed using P1 exhibited significant deformation in the first heating stage, and little deformation occurred in the second heating stage. In contrast, the

 doi:10.20944/preprints202407.1924.v1

sample printed using P2 displayed minimal deformation in the first heating stage, but underwent severe softening deformation in the second heating stage. For the sample printed using C, although it experienced noticeable softening deformation in both stages, its final deformation degree was significantly lower than that of the samples printed using P1 and P2.

The unique behavior of the sample printed using C can be ascribed to the composite structure. During the first heating stage, the P1 component melted, while most of the P2 component remained solid, acting as rigid particles and providing reinforcement. This structural characteristic effectively reduced the deformation rate, resulting in a significantly smaller deformation compared with the sample printed using pure P1, as presented in Figure 11. Upon entering the second heating stage, the P1 component had already cured, and the P2 component began to melt. At this time, the cured P1 component played the role of reinforcing agent, leading to a smaller deformation at this stage compared with the sample printed using pure P2, as shown in Figure 11. In general, the excellent resistance to softening deformation exhibited by the sample printed using C throughout the entire heating process is due to the structural support provided by the unmelted P2 component and the cured P1 component in the first and second heating stages, respectively.

To assess the evolution of mechanical properties throughout the forming process, Vickers hardness tests were employed, as presented in Figure 12. Preliminary results showed no significant hardness differences between the samples printed using P1, P2, and C and their respective original powders. This observation suggests that although high-velocity particle impacted during the CSAM process leading to partial decomposition of latent curing agents, no substantial curing reaction was triggered.

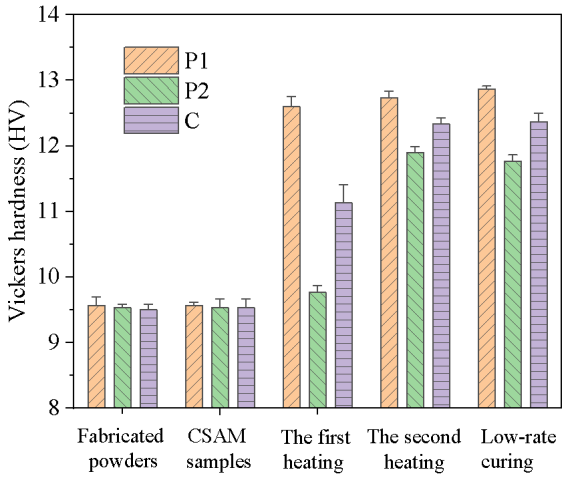

Figure 12. The Vickers hardness evolution of P1, P2, and C powders and printed parts before heating, after the first heating at 85 °C for 1 h, after the second heating at 150 °C for 0.5 h, and after full curing by slow heating from 50 °C to 150 °C with a rate of 0.1 °C/min.

During the subsequent stepwise heat treatment, the materials exhibited distinct behavioral patterns. After the first heating stage (85 °C, 1 h), P1 demonstrated a significant increase in Vickers hardness, indicating that the curing reaction effectively enhanced its mechanical properties. In contrast, P2 showed only a slight increase in hardness at this stage, suggesting that its primary curing reaction had not yet initiated. In the second heating stage (150 °C, 30 mins), the hardness of P1 increased marginally, indicating that its curing reaction was almost completed in the first stage. Conversely, P2 underwent a significant hardness enhancement during this stage, revealing the occurrence of its melting and curing processes. Notably, the hardness characteristics of the composite material C was gradually improved, correlated with the increase of the hardness of P1 and P2. This phenomenon reflects the gradual enhancement of mechanical properties in the composite material during the stepwise curing process. Ultimately, the hardness of composite material C after stepwise curing was comparable to that of samples cured using a low-rate heating process. It demonstrates

 doi:10.20944/preprints202407.1924.v1

that the stepwise curing technique not only obtains the same mechanical properties as the traditional low-rate heating methods, but also significantly reduces the heating time.

4. Conclusions

This study presents a novel approach to address the softening deformation issue encountered with thermosetting materials in additive manufacturing. It consists of three key components, i.e., the development of a composite thermosetting powder containing materials with different curing temperatures, the utilization of CSAM for fabrication, and the implementation of a stepwise curing process to sequentially cure each component of the composite material.

The efficacy of this approach was validated through case studies involving the fabrication of two distinct single-component thermosetting powders and their composite powder. During the CSAM process, all powders successfully produced cylindrical samples that maintained their solid state throughout the printing process. During the stepwise curing process, the samples printed using composite material demonstrated superior resistance to deformation compared to its single-component counterparts. This enhanced performance was attributed to the unique characteristic of the composite that allows some of its components in a solid state while others melt, providing structural support and minimizing softening deformation. Furthermore, the stepwise isothermal curing process proved more time-efficient than traditional low heating rate curing methods.

It is expected that increasing the variety of thermosetting materials and ensuring an equal proportion of each component during the stepwise curing process will further enhance the proportion of solid materials. This improvement will increase resistance to softening deformation, making the approach suitable for applications demanding higher strength requirements.

Author Contributions: Conceptualization, B.H.; methodology, B.H.; formal analysis, K.W.; investigation, B.H.; resources, P.G.; writing—original draft preparation, B.H.; writing—review and editing, K.W., Y.L., S.R.; visualization, B.H.; supervision, K.W., Y.L., P.G.; funding acquisition, P.G. All authors have read and agreed to the published version of the manuscript.

Funding: This research was funded by the National Natural Science Foundation of China received by Prof. Kaifeng Wang, grant number 52075367.

Data Availability Statement: Data are contained within the article.

Acknowledgments: The authors from Tianjin University acknowledge the financial support partially by Prof. Kaifeng Wang.

Conflicts of Interest: The authors declare no conflict of interest.

References

1. D'Aloia, A.G.; Proietti, A.; Bidsorkhi, H.C.; Tamburrano, A.; Bellis, G. de; Marra, F.; Bregnocchi, A.; Sarto, M.S. Electrical, Mechanical and Electromechanical Properties of Graphene-Thermoset Polymer Composites Produced Using Acetone-DMF Solvents. *Polymers* **2018**, *10*, 82. https://doi.org/10.3390/polym10010082.
2. Daungkumsawat, J.; Okhawilai, M.; Charoensuk, K.; Prastowo, R.B.; Jubsilp, C.; Karagiannidis, P.; Rimdusit, S. Development of Lightweight and High-Performance Ballistic Helmet Based on Poly(Benzoxazine-co-Urethane) Matrix Reinforced with Aramid Fabric and Multi-Walled Carbon Nanotubes. *Polymers* **2020**, *12*, 2897. https://doi.org/10.3390/polym12122897.
3. Morici, E.; Dintcheva, N.T. Recycling of Thermoset Materials and Thermoset-Based Composites: Challenge and Opportunity. *Polymers* **2022**, *14*, 4153. https://doi.org/10.3390/polym14194153.
4. Han, D.; Yang, C.; Fang, N.X.; Lee, H. Rapid multi-material 3D printing with projection micro-stereolithography using dynamic fluidic control. *Addit. Manuf.* **2019**, *27*, 606–615. https://doi.org/10.1016/j.addma.2019.03.031.
5. Sano, Y.; Matsuzaki, R.; Ueda, M.; Todoroki, A.; Hirano, Y. 3D printing of discontinuous and continuous fibre composites using stereolithography. *Addit. Manuf.* **2018**, *24*, 521–527. https://doi.org/10.1016/j.addma.2018.10.033.
6. Lei, D.; Yang, Y.; Liu, Z.; Chen, S.; Song, B.; Shen, A.; Yang, B.; Li, S.; Yuan, Z.; Qi, Q.; et al. A general strategy of 3D printing thermosets for diverse applications. *Mater. Horiz.* **2019**, *6*, 394–404. https://doi.org/10.1039/c8mh00937f.

7. Yuan, J.; Chen, C.; Yao, D.; Chen, G. 3D Printing of Oil Paintings Based on Material Jetting and Its Reduction of Staircase Effect. *Polymers* **2020**, *12*, 2536. https://doi.org/10.3390/polym12112536.
8. Tamez, M.B.A.; Taha, I. A review of additive manufacturing technologies and markets for thermosetting resins and their potential for carbon fiber integration. *Addit. Manuf.* **2021**, *37*, 101748. https://doi.org/10.1016/j.addma.2020.101748.
9. Jiang, P.; Ji, Z.; Zhang, X.; Liu, Z.; Wang, X. Recent advances in direct ink writing of electronic components and functional devices. *Prog. Addit. Manuf.* **2018**, *3*, 65–86. https://doi.org/10.1007/s40964-017-0035-x.
10. Casanova-Batlle, E.; Guerra, A.J.; Ciurana, J. Continuous Based Direct Ink Write for Tubular Cardiovascular Medical Devices. *Polymers* **2020**, *13*, 77. https://doi.org/10.3390/polym13010077.
11. Rosenthal, M.; Henneberger, C.; Gutkes, A.; Bues, C.-T. Liquid Deposition Modeling: A promising approach for 3D printing of wood. *Eur. J. Wood Prod.* **2018**, *76*, 797–799. https://doi.org/10.1007/s00107-017-1274-8.
12. Yang, H.; Ji, F.; Li, Z.; Tao, S. Preparation of Hydrophobic Surface on PLA and ABS by Fused Deposition Modeling. *Polymers* **2020**, *12*, 1539. https://doi.org/10.3390/polym12071539.
13. Compton, B.G.; Lewis, J.A. 3D-printing of lightweight cellular composites. *Adv. Mater.* **2014**, *26*, 5930–5935. https://doi.org/10.1002/adma.201401804.
14. Zeng, Z.; Deng, X.; Cui, J.; Jiang, H.; Yan, S.; Peng, B. Improvement on Selective Laser Sintering and Post-Processing of Polystyrene. *Polymers* **2019**, *11*, 956. https://doi.org/10.3390/polym11060956.
15. Wudy, K.; Drummer, D. Infiltration Behavior of Thermosets for Use in a Combined Selective Laser Sintering Process of Polymers. *JOM* **2019**, *71*, 920–927. https://doi.org/10.1007/s11837-018-3226-0.
16. Burgos Pintos, P.; Moreno Sánchez, D.; Delgado, F.J.; Sanz de León, A.; Molina, S.I. Influence of the Carbon Fiber Length Distribution in Polymer Matrix Composites for Large Format Additive Manufacturing via Fused Granular Fabrication. *Polymers* **2023**, *16*, 60. https://doi.org/10.3390/polym16010060.
17. Fontana, L.; Giubilini, A.; Arrigo, R.; Malucelli, G.; Minetola, P. Characterization of 3D Printed Polylactic Acid by Fused Granular Fabrication through Printing Accuracy, Porosity, Thermal and Mechanical Analyses. *Polymers* **2022**, *14*, 3530. https://doi.org/10.3390/polym14173530.
18. Li, W.; Yang, K.; Yin, S.; Yang, X.; Xu, Y.; Lupoi, R. Solid-state additive manufacturing and repairing by cold spraying: A review. *J. Mater. Sci. Technol.* **2018**, *34*, 440–457. https://doi.org/10.1016/j.jmst.2017.09.015.
19. Bagherifard, S.; Monti, S.; Zuccoli, M.V.; Riccio, M.; Kondás, J.; Guagliano, M. Cold spray deposition for additive manufacturing of freeform structural components compared to selective laser melting. *Mater. Sci. Eng. A Struct. Mater.* **2018**, *721*, 339–350. https://doi.org/10.1016/j.msea.2018.02.094.
20. Ravi, K.; Deplancke, T.; Ogawa, K.; Cavaillé, J.-Y.; Lame, O. Understanding deposition mechanism in cold sprayed ultra high molecular weight polyethylene coatings on metals by isolated particle deposition method. *Addit. Manuf.* **2018**, *21*, 191–200. https://doi.org/10.1016/j.addma.2018.02.022.
21. Khalkhali, Z.; Rothstein, J.P. Characterization of the cold spray deposition of a wide variety of polymeric powders. *Surf. Coat. Technol.* **2020**, *383*, 125251. https://doi.org/10.1016/j.surfcoat.2019.125251.
22. ASTM E384-17. *Standard Test Method for Microindentation Hardness of Materials;* ASTM International: West Conshohocken, PA, 2017.
23. Sova, A.; Kosarev, V.F.; Papyrin, A.; Smurov, I. Effect of Ceramic Particle Velocity on Cold Spray Deposition of Metal-Ceramic Coatings. *J. Therm. Spray Tech.* **2011**, *20*, 285–291. https://doi.org/10.1007/s11666-010-9571-3.
24. Winnicki, M. Advanced Functional Metal-Ceramic and Ceramic Coatings Deposited by Low-Pressure Cold Spraying: A Review. *Coatings* **2021**, *11*, 1044. https://doi.org/10.3390/coatings11091044.
25. Assadi, H.; Schmidt, T.; Richter, H.; Kliemann, J.-O.; Binder, K.; Gärtner, F.; Klassen, T.; Kreye, H. On Parameter Selection in Cold Spraying. *J. Therm. Spray Tech.* **2011**, *20*, 1161–1176. https://doi.org/10.1007/s11666-011-9662-9.
26. Grujicic, M.; Zhao, C.; Tong, C.; DeRosset, W.; Helfritch, D. Analysis of the impact velocity of powder particles in the cold-gas dynamic-spray process. *Mater. Sci. Eng. A Struct. Mater.* **2004**, *368*, 222–230. https://doi.org/10.1016/j.msea.2003.10.312.
27. Zahiri, S.H.; Antonio, C.I.; Jahedi, M. Elimination of porosity in directly fabricated titanium via cold gas dynamic spraying. *J. Mater. Process Technol.* **2009**, *209*, 922–929. https://doi.org/10.1016/j.jmatprotec.2008.03.005.
28. Ren, Y.Q.; King, P.C.; Yang, Y.S.; Xiao, T.Q.; Chu, C.; Gulizia, S.; Murphy, A.B. Characterization of heat treatment-induced pore structure changes in cold-sprayed titanium. *Mater. Charact.* **2017**, *132*, 69–75. https://doi.org/10.1016/j.matchar.2017.08.006.
29. Hong, B.; Wang, K.; Gu, P. Cold Spray-Based Additive Manufacturing of Thermosets. *J. Therm. Spray Tech.* **2022**, *31*, 2003–2012. https://doi.org/10.1007/s11666-022-01428-7.
30. Wicks, D.A.; Wicks, Z.W. Blocked isocyanates III: Part A. Mechanisms and chemistry. *Prog. Org. Coat.* **1999**, *36*, 148–172. https://doi.org/10.1016/S0300-9440(99)00042-9.

 doi:10.20944/preprints202407.1924.v1